MNRAS **000**, 1–14 (2017) Preprint 11 April 2017 Compiled using MNRAS LATEX style file v3.0

The Ultraviolet Spectroscopic Evolution of the Low-Luminosity Tidal Disruption Event iPTF16fnl

J. S. Brown[1]*, C. S. Kochanek[1,2], T. W.-S. Holoien[1,2], K. Z. Stanek[1,2], K. Auchettl[2,3], B. J. Shappee[4,5,6], J. L. Prieto[7,8], N. Morrell[9], E. Falco[10], J. Strader[11], L. Chomiuk[11], R. Post[12], S. Villanueva Jr.[1], S. Mathur[1,2], S. Dong[13], P. Chen[13], and S. Bose[13]

[1] *Department of Astronomy, The Ohio State University, 140 West 18th Avenue, Columbus, OH 43210, USA*
[2] *Center for Cosmology and Astro-Particle Physics, The Ohio State University, 191 West Woodruff Avenue, Columbus, OH 43210, USA*
[3] *Department of Physics, The Ohio State University, 191 W. Woodruff Avenue, Columbus, OH 43210, USA*
[4] *Carnegie Observatories, 813 Santa Barbara Street, Pasadena, CA 91101, USA*
[5] *Hubble Fellow*
[6] *Carnegie-Princeton Fellow*
[7] *Núcleo de Astronomía de la Facultad de Ingeniería y Ciencias, Universidad Diego Portales, Av. Ejército 441, Santiago, Chile*
[8] *Millennium Institute of Astrophysics, Santiago, Chile*
[9] *Las Campanas Observatory, Carnegie Observatories, Casilla 601, La Serena, Chile*
[10] *Harvard-Smithsonian Center for Astrophysics, 60 Garden St., Cambridge, MA 02138, USA*
[11] *Department of Physics and Astronomy, Michigan State University, East Lansing, MI 48824*
[12] *Post Observatory, Lexington, MA 02421*
[13] *Kavli Institute for Astronomy and Astrophysics, Peking University, Yi He Yuan Road 5, Hai Dian District, Beijing 100871, China*

arXiv:1704.02321v1 [astro-ph.HE] 7 Apr 2017

Accepted XXX. Received YYY; in original form ZZZ

ABSTRACT

We present the ultraviolet (UV) spectroscopic evolution of a tidal disruption event (TDE) for the first time. After the discovery of the nearby TDE iPTF16fnl, we obtained a series of observations with the Space Telescope Imaging Spectrograph (STIS) onboard the Hubble Space Telescope (HST). The dominant emission features closely resemble those seen in the UV spectra of the TDE ASASSN-14li and are also similar to those of N-rich quasars. However, there is significant evolution in the shape and central wavelength of the line profiles over the course of our observations, such that at early times the lines are broad and redshifted, while at later times the lines are significantly narrower and peak near the wavelengths of their corresponding atomic transitions. Like ASASSN-14li, but unlike N-rich quasars, iPTF16fnl shows neither Mg II λ2798Å nor C III] λ1909Å emission features. We also present optical photometry and spectroscopy, which suggest that the complex He II profiles observed in the optical spectra of many TDEs are in part due to the presence of N III and C III Wolf-Rayet features, which can potentially serve as probes of the far-UV when space-based observations are not possible. Finally, we use *Swift* XRT and UVOT observations to place strong limits on the X-ray emission and determine the characteristic temperature, radius, and luminosity of the emitting material. We find that iPTF16fnl is subluminous and evolves more rapidly than other optically discovered TDEs.

Key words: accretion, accretion disks – black hole physics – galaxies: nuclei

1 INTRODUCTION

When a star passes through the center of a galaxy, it may be disrupted by the central supermassive black hole (SMHB) in a "tidal disruption event" (TDE). After the disruption of a main sequence star, approximately half of the stellar debris will remain on bound orbits and asymptotically return to pericenter at a rate proportional to $t^{-5/3}$ (Rees 1988; Evans & Kochanek 1989; Phinney 1989). While the first TDEs were discovered as X-ray transients (e.g. Grupe, Thomas & Leighly 1999; Komossa & Bade 1999; Komossa & Greiner 1999), the increasing number of wide-

*E-mail: brown@astronomy.ohio-state.edu

© 2017 The Authors

field optical transient surveys have led to more recent TDEs being discovered as luminous blue flares from otherwise passive galactic nuclei (Gezari et al. 2012; Arcavi et al. 2014; Holoien et al. 2014).

TDEs are a highly inhomogenous class of objects. The optical spectra and X-ray properties in particular are highly diversified (e.g Gezari et al. 2012; Holoien et al. 2014; Arcavi et al. 2014; Vinkó et al. 2015; Holoien et al. 2016b,a; Auchettl, Guillochon & Ramirez-Ruiz 2016). Furthermore, the evolutionary timescales, peak luminosities, and spectral energy distributions of optical TDEs vary considerably from one TDE to the next (e.g., Gezari et al. 2015; Brown et al. 2016a,b; Holoien et al. 2016a). Despite their non-uniform characteristics, all optically discovered TDEs are associated with a hot (tens of thousands of Kelvin) and luminous ($L \gtrsim 10^{40}$ ergs s^{-1}) flare from an otherwise non-active galactic nuclei. While TDEs are now most freqently discovered in optical transient surveys, energetically speaking, they are predominantly ultraviolet (UV) phenomena. While many TDEs have been monitored with broadband UV filters, UV spectra can reveal much more about the kinematics and ionization structure of the debris. Cenko et al. (2016) obtained HST/STIS spectra of what was, at the time, the closest TDE ever discovered (ASASSN-14li; Holoien et al. 2016b). Their observations revealed the presence of highly ionized, broad C, N, and Si emission, in addition to ionized H and He that had been previously observed in the optical. The lack of Mg II emission, a feature universally seen in AGN/quasar spectra, was also particularly interesting.

The transient iPTF16fnl was discovered on 2016-08-26 and was promptly classified as a TDE on 2016-08-31 (Gezari et al. 2016). The position of the transient (J2000 RA/Dec = 00:29:57.04 +32:53:37.5) is consistent with the center of the galaxy Mrk 0950 at a redshift of $z = 0.0163$, corresponding to a luminosity distance of $d = 67.8$ Mpc ($H_0 = 73$ km s^{-1} Mpc^{-1}, $\Omega_M = 0.27$, $\Omega_\Lambda = 0.73$). In the discovery paper, Blagorodnova et al. (2017) analyzed the photometric evolution and optical spectroscopy and demonstrated that iPTF16fnl is indeed a rapidly evolving, low luminosity TDE. Our analysis was carried out independently, and is broadly consistent with the results of that paper, though there are some important differences. After Gezari et al. (2016) classified the transient as a TDE, we inspected the reported location in ASAS-SN data and found a transient near our sensitivity limit. Since the transient exceeded our triggering criteria, was very nearby, and was apparently brightening, we triggered our HST ToO program and obtained 3 HST/STIS UV spectra of the TDE over the course of the following six weeks. We also obtained *Swift* observations, ground-based photometric monitoring, and optical spectra probing the early and late phases of the event.

In this paper, we present the results of this observing campaign. In Section 2 we present UV spectra taken with HST/STIS alongside broadband X-ray, UV, and optical photometry. In Section 3 we use our observational data to model the physical nature of the transient, and also place a stringent upper limit on the X-ray emission from the TDE. In Section 4 we and summarize our results and discuss the most important implications of our findings.

Table 1. Photometry of Mrk 0950

Filter	Magnitude	Magnitude Uncertainty
FUV	21.10	0.27
NUV	19.87	0.08
u	17.62	0.01
g	16.08	0.01
r	15.49	0.01
i	15.18	0.01
z	14.92	0.01
J	14.69	0.05
H	14.47	0.05
K_s	14.68	0.05

These are 5.″0 radius aperture magnitudes from GALEX, SDSS, and 2MASS. Magnitudes are in the AB system.

2 OBSERVATIONS

Once the transient iPTF16fnl was classified as a TDE, we initiated a follow-up campaign in order to study in detail the nearest TDE yet discovered. In this Section we summarize the observational data used in our analysis.

2.1 Archival Host Data

In order to constrain the properties of the host galaxy, we performed a search of archival databases for observations of Mrk 0950. We retrieved archival *ugriz* images of Mrk 0950 from the Twelfth Data Release of the Sloan Digital Sky Survey (SDSS; Alam et al. 2015). We also retrieved near-IR JHK_s Two-Micron All Sky Survey (2MASS; Skrutskie et al. 2006) images of the host, as well as UV imaging from the Galaxy Evolution Explorer (GALEX; Martin et al. 2005). The AllWISE color of $W1 - W2 = 0.01 \pm 0.05$ (Cutri & et al. 2014) indicates that Mrk 0950 lacks a strong AGN component (Stern et al. 2012; Assef et al. 2013). We examine images from the *ROSAT* All-Sky Survey (RASS; Voges et al. 1999) and derive an upper limit on the count rate in the 0.3–10 keV band of $< 1.9 \times 10^{-2}$ counts s^{-1}. This corresponds to a limit on the unabsorbed flux of $\sim 2 \times 10^{-13}$ ergs s^{-1} cm $^{-2}$ ($L_X \lesssim 1.1 \times 10^{41}$ ergs s^{-1}), which provides further evidence that Mrk 0950 lacks a strong AGN. We performed aperture photometry on the GALEX, SDSS, and 2MASS images and measured the flux enclosed in a 5.″0 aperture. We present the host magnitudes derived from the archival data in Table 1.

There are no archival Spitzer, Herschel, HST, Chandra, or X-ray Multi-Mirror Mission (XMM-Newton) observations of Mrk 0950, and there are no radio sources listed at this position in the FIRST (Becker, White & Helfand 1995) or NVSS (Condon et al. 1998) catalogs.

We modeled the host galaxy SED with the Fitting and Assessment of Synthetic Templates (FAST; Kriek et al. 2009), using the fluxes derived from the GALEX, SDSS, and 2MASS archival images. We assumed a Cardelli, Clayton & Mathis (1989) extinction law with $R_V = 3.1$ and Galactic extinction of $A_V = 0.22$ (Schlafly & Finkbeiner 2011), an exponentially declining star-formation history, a Salpeter IMF, and the Bruzual & Charlot (2003) stellar population models. We obtained a reasonable fit ($\chi^2_\nu = 0.98$) which yielded the follow-

ing parameters: $M_* = (2.34^{+0.61}_{-0.05}) \times 10^9 M_\odot$, age$= 1.29^{+0.33}_{-0.03}$ Gyr, and a 1-σ upper limit on the star formation rate of SFR< 0.007 $M_\odot$ yr^{-1}.

There are no black hole mass measurements for this galaxy in the literature. In order to obtain an estimate of the black hole mass, we adopt an upper limit on the bulge mass using the stellar mass derived from the photometry in the central 5″ of the galaxy. This a reasonable approximation given the properties of the light profile measured from the SDSS imaging (i.e. half light radius $\sim 3\farcs5$). We then adopt the $M_{\rm bulge}$–$M_{\rm BH}$ scaling relation from McConnell & Ma (2013) and estimate the mass of the black hole to be $M_{\rm BH} \lesssim 5.5 \times 10^6 M_\odot$. Thus the black hole is not so massive that a main sequence star would simply be absorbed by the SMBH before being tidally disrupted. Given the lack of archival spectra, we will address the spectroscopic nature of the host in Section 3.

2.2 ASAS-SN Detection

After the discovery of the transient was announced (Gezari et al. 2016), we examined the location of the object in ASAS-SN data. The last ASAS-SN epoch before discovery was observed on UT 2016-08-26.51 under moderate conditions by the quadruple 14-cm "Brutus" telescope in Haleakala, Hawaii. This ASAS-SN field was processed by the standard ASAS-SN pipeline (Shappee et al. 2014) using the *isis* image subtraction package (Alard & Lupton 1998; Alard 2000), except we took extra care to exclude images with flux from iPTF16fnl from the construction of the reference image. We performed aperture photometry at the location of iPTF16fnl on the subtracted images using the IRAF *apphot* package and calibrated the results using the AAVSO Photometric All-Sky Survey (APASS; Henden et al. 2016). We have detections of the transient on UT 2016-08-26.51 ($V = 17.96 \pm 0.24$), and on UT 2016-08-30.52 ($V = 17.49 \pm 0.18$). We do not detect the object in images taken before UT 2016-08-26.51, but our limits preceeding the discovery of the transient are relatively shallow ($V \gtrsim 17$), so this is not to say the transient is not present at earlier epochs.

2.3 HST/STIS ToO Observations

We observed iPTF16fnl using STIS and the FUV/NUV MAMA detectors. We used the $52\farcs0 \times 0\farcs2$ slit and the G140L (1425Å, FUV-MAMA) and G230L (2736Å, NUV-MAMA) gratings. The visits were obtained over 1, 2 and 4 orbits, respectively, as the target faded. The integration times were 792 seconds (FUV and NUV) in four equal exposures (each setting) for the first visit, 1854 (FUV) and 2466 (NUV) seconds in six exposures for the second visit, and 4785 (FUV) and 5500 (NUV) seconds in ten roughly equal exposures for the third visit. A cosmic ray CR-SPLIT image pair was obtained at each dither position and the telescope was dithered along the slit by 16 pixels. Since the trace of iPTF16fnl was clearly present in the two-dimensional frames and spatially unresolved, we use the one-dimentional spectra output by the HST pipeline. For each epoch, we perform inverse-variance-weighted combinations of the one-dimensional spectra and merge the FUV and NUV channels. We correct for Galactic reddening assuming $A_V = 0.22$ and $R_V = 3.1$ (O'Donnell 1994; Schlafly & Finkbeiner 2011). The merged spectra are shown in Figure 1.

2.4 *Swift* Observations

We also obtained *Swift* observations of iPTF16fnl. The UVOT (Roming et al. 2005) observations were obtained in six filters: V (5468 Å), B (4392 Å), U (3465 Å), $UVW1$ (2600 Å), $UVM2$ (2246 Å), and $UVW2$ (1928 Å). We used the UVOT software task UVOTSOURCE to extract the source counts from a $5\farcs0$ radius region and a sky region with a radius of $\sim 40''$. The UVOT count rates were converted into magnitudes and fluxes based on the most recent UVOT calibration (Poole et al. 2008; Breeveld et al. 2010). The observed UVOT magnitudes are shown in Figure 4 and are tabulated in Table A1.

We simultaneously obtained *Swift* X-ray Telescope (XRT; Burrows et al. 2005) observations of the source. The XRT was run in photon-counting (PC) mode (Hill et al. 2004) which is the standard imaging mode of the XRT. We reduced all observations following the *Swift* XRT data reduction guide[1] and reprocessed the level one XRT data using the *Swift xrtpipeline* version 0.13.2 script, producing cleaned event files and exposure maps for each observation.

To extract the number of background subtracted source counts in the 0.3–10.0 keV energy band from each individual observation, we used a source region centered on the position of iPTF16fnl with a radius of 50″ and a source free background region centered at $(\alpha, \delta) = (00^h29^m25.5^s, +32°51'15.6'')$ with a radius of 200″. We correct for Galactic absorption assuming a column density of 5.6×10^{20} cm^{-2} (Kalberla et al. 2005).

2.5 Ground-Based Monitoring

In addition to space-based observations, we also obtained ground based photometric and spectroscopic monitoring of iPTF16fnl for approximately 4 months following discovery. The photometric monitoring consisted of $BgVri$ imaging, which we obtained from several telescopes including 1-m telescopes on the Las Cumbres Observatory telescope network Brown et al. (2013), the 20-in DEMONEXT telescope (Villanueva et al. 2016), and the 24-in telescope at Post Observatory. We measured aperture photometry with the same $5\farcs0$ aperture radius used for both the *Swift* and archival host photometry. Photometric zero-points were determined using nearby stars with SDSS and/or APASS magnitudes.

We also obtained several early ($t \lesssim 14$ days) optical spectra of iPTF16fnl, as well as late-time spectra taken after the transient had faded considerably. The early time spectra were obtained with the FAST Spectrograph (FAST; Fabricant et al. 1998) on the Fred L. Whipple Observatory Tillinghast 1.5-m telescope, the Wide Field Reimaging CCD Camera (WFCCD) mounted on the Las Campanas Observatory du Pont 2.5-m telescope, and the Goodman Spectrograph on the Southern Astrophysical Research (SOAR) 4.1-m telescope. The late-time spectra were obtained with the Multi-Object Double Spectrographs (MODS; Pogge et al.

[1] http://swift.gsfc.nasa.gov/analysis/xrt_swguide_v1_2.pdf

2010) mounted on the dual 8.4-m Large Binocular Telescope (LBT) on Mt. Graham. The MODS data were reduced with a combination of the MODSCCDRED[2] PYTHON package and the MODSIDL pipeline[3]. The other spectroscopic data were reduced using standard techniques in IRAF. While there are slight difference in the wavelength coverage and resolution of the spectrographs, the spectra cover the majority of the optical bandpass ($\sim$ 3000Å to $\gtrsim$ 7000Å) and have a resolution of $\sim$ 5Å. Finally, in order to facilitate comparison of spectra across multiple observing epochs and instruments, we flux-calibrated each spectra with contemporaneous r-band imaging.

3 ANALYSIS

In this section we present the evolution of iPTF16fnl from $\sim$ 1200Å up to $\sim$ 8000Å. This is the first time the temporal evolution of a TDE has been spectroscopically observed in the the UV, and provides key constraints for theories attempting to explain the observed properties of TDEs.

3.1 Spectroscopic Analysis

The spectroscopic evolution of iPTF16fnl in the UV is shown in Figure 1. Each spectrum is shown in a color corresponding to the observation date. The squares show the contemporaneous *Swift* observations, which, for purposes of comparison, we have used to set the overall normalization of the HST/STIS spectra. The gray line shows the best fit SED based on the archival host data, while the dashed curves show our blackbody fits to the host-subtracted UVOT fluxes (see Section 3.2). Prominent atomic transitions are labeled, and the portion of the spectrum affected by geocoronal airglow is marked with the telluric symbol.

We emphasize that the HST/STIS and *Swift* observations sample different regions of the galaxy and thus have different levels of host contamination. The spectrum is dominated by the blue emission of the TDE at the very center of the galaxy, while the modeling of the host is based on the central 5″ of the galaxy. Thus a direct comparison between the two is not possible since the contribution of the host in the HST spectra is not precisely known. However, a relative comparison between the observed *Swift* fluxes, the archival host SED, and our blackbody fits is fair and demostrates the relative contribution of the host and TDE to the observed broadband flux at each epoch.

Our first spectrum of iPTF16fnl bears a strong resemblance to that of ASASSN-14li from Cenko et al. (2016). Both objects are well approximated by a combination of blackbody continuum emission with a temperature of a few 10^4 K, coupled with broad emission and narrow absorption associated with highly ionized atomic transitions. Our blackbody fits agree well with the shape of the UV spectra, and the best agreement is seen at earlier times when the flux from the TDE dominates the observed UV emission and the contribution from the underlying host is negligible. At later times, as the transient fades, the observed (host+TDE) spectrum begins to diverge from our blackbody fits because the host contribution (which we subtract before modeling the excess emission) becomes more significant.

The line profiles are complex; absorption and emission features of multiple lines are blended together and also frequently coincide with Galactic absorption features. In the earlier spectra, the emission features are systematically redshifted relative to the line center. For instance, the peak of the N V feature is redshifted by $\sim 2000 - 2500$ km s^{-1}, as is that of C IV. Some lower ionization features (e.g. N III]) show no apparent redshift at all. The He II profile is particularly interesting. While the emission peaks near the transition wavelength at 1640Å, there is a significant component of the line profile that extends to redder wavelengths. This suggests that the distribution of the highly ionized metals may differ from that of the gas producing the bulk of the lower ionization features. However, given the complex nature of the line blending, it is difficult to differentiate between this scenario and one in which the high ionization lines are systematically broader and/or happen to coincide with more absorption features at shorter wavelengths. In fact, the Si IV and C IV show clear blueshifted absorption troughs ($\Delta v \sim$ FWHM $\sim$ 6000 km s^{-1}) that may signify an outflow, and also likely contribute to the apparent redshift of the emission line profiles. Additionally, there is a non-negligible amount of Galactic extinction along the line of sight ($A_V = 0.22$), and nearly all identified line profiles in Figures 1 and 2 have relatively strong Galactic absorption features located blueward of the transition wavelength in the rest frame of the TDE, as was also observed by Cenko et al. (2016) for ASASSN-14li.

The shapes of the line profiles vary with time. This includes the apparent width of the lines, as well as their peak wavelengths. The systematic redshift observed in N V, Si IV, and C IV at early times is less dramatic in the last HST/STIS spectrum, and the broad absorption features are also less apparent at late times. There is an apparent decrease in flux in the region between Lyα and N V λ1240Å. While this region is affected by geocoronal afterglow, the latest spectrum shows a substantial drop in flux in this region relative to the previous two. We also note the sudden appearance of the N IV] λ1486Å line, which was relatively weak in the initial HST/STIS spectrum but quite prominent in the last spectrum. Similarly, the He II line becomes much stronger at later times relative to the apparent continuum, and by $\sim$ 50 days the profile is strongly peaked at the transition wavelength. The evolution of the spectra can be explained in large part by the narrowing of the emission lines as the flare fades. This is opposite the behavior seen in actively accreting SMBHs (McGill et al. 2008; Denney et al. 2009), but appears to be typical of TDEs (e.g., Holoien et al. 2014, 2016b,a; Brown et al. 2016a,b). The increasing equivalent width of the He II feature indicates that it is not fading as fast as the other lines. This may also suggest that the bulk of the He II emission is produced by gas that evolves on a longer timescale than the gas producing the highly ionized metal lines. The wavelengths of the narrow absorption features remain constant, while the velocity offsets and widths of the broad absorption features appear to decrease with time. This likely indicates that material responsible for the narrow absorption features is located at larger distances and

[2] http://www.astronomy.ohio-state.edu/MODS/Software/modsCCDRed/
[3] http://www.astronomy.ohio-state.edu/MODS/Software/modsIDL/

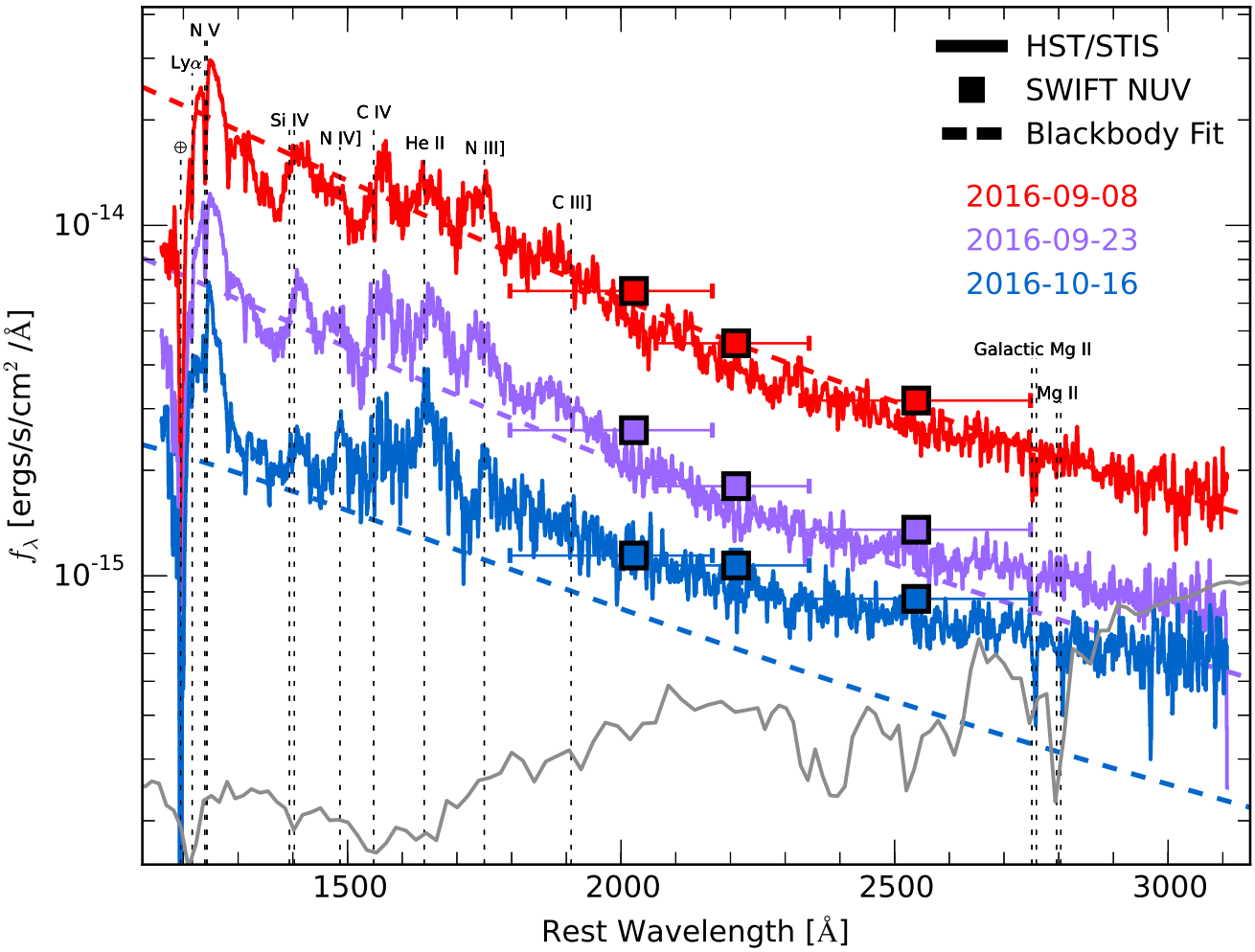

Figure 1. The UV evolution of iPTF16fnl as revealed by HST/STIS spectra and *Swift* photometry. The spectra have been smoothed with a 5 pixel boxcar and scaled by a constant factor to best match the *Swift* photometry for ease of comparison. The dashed lines show our blackbody fits to the host subtracted *Swift* fluxes. Prominent atomic transitions are marked with vertical dotted lines. The thin gray line shows our estimate of the UV spectrum of the host based on the SED model.

varies on significantly longer timescales than the material responsible for the broad features.

Figure 2 shows the blue portion of the iPTF16fnl HST/STIS spectrum compared to that of ASASSN-14li from Cenko et al. (2016). The spectra have been scaled by a constant factor for ease of comparison. The phase of the ASASSN-14li spectrum most closely matches that of our last HST spectrum, though the phases of the two are not necessarily comparable given the uncertainty on the rise times. The spectra are shown in the rest frame of the respective TDEs. Due to the different redshifts of the two objects, Galactic absorption features in the ASASSN-14li spectrum are located at systematically shorter wavelengths than their counterparts in the iPTF16fnl spectrum. This includes the geocoronal afterglow which strongly affects the Lyα portion of the iPTF16fnl spectrum, but has a subtler effect on the ASASSN-14li spectrum. Nonetheless, both spectra show the same set of prominent emission features. The line profiles of ASASSN-14li most closely resemble those in the latest iPTF16fnl spectrum, which is not necessarily surprising given the timing of the observations. Specifically, both the ASASSN-14li spectrum and our latest spectrum of iPTF16fnl show little evidence of the strongly redshifted emission profiles that are so apparent in the early time iPTF16fnl spectrum.

Interestingly, neither ASASSN-14li nor iPTF16fnl show the Mg II emission typically associated with accreting SMBHs. The Mg II emission comes from the relatively large partially ionized regions in AGN (e.g. Peterson 1993; Richards et al. 2002). The absence of Mg II emission in TDEs could be a symptom of the shape of the radiation field, or it could indicate that the nebula is matter bounded and the Mg is predominantly in higher ionization states. The ionization energy of Mg II is low enough ($E_{\rm ion}$ = 15.03 eV) for this to be plausible. Like Mg II, He I emission is typically quite strong in the spectrum of quasars, but is relatively weak in the spectra of TDEs. In the SDSS quasar composite spectrum from Vanden Berk et al. (2001), the He I λ5877Å flux is a factor of a few larger than the He II λ4686Å flux. However, ASASSN-14li and iPTF16fnl show evidence for

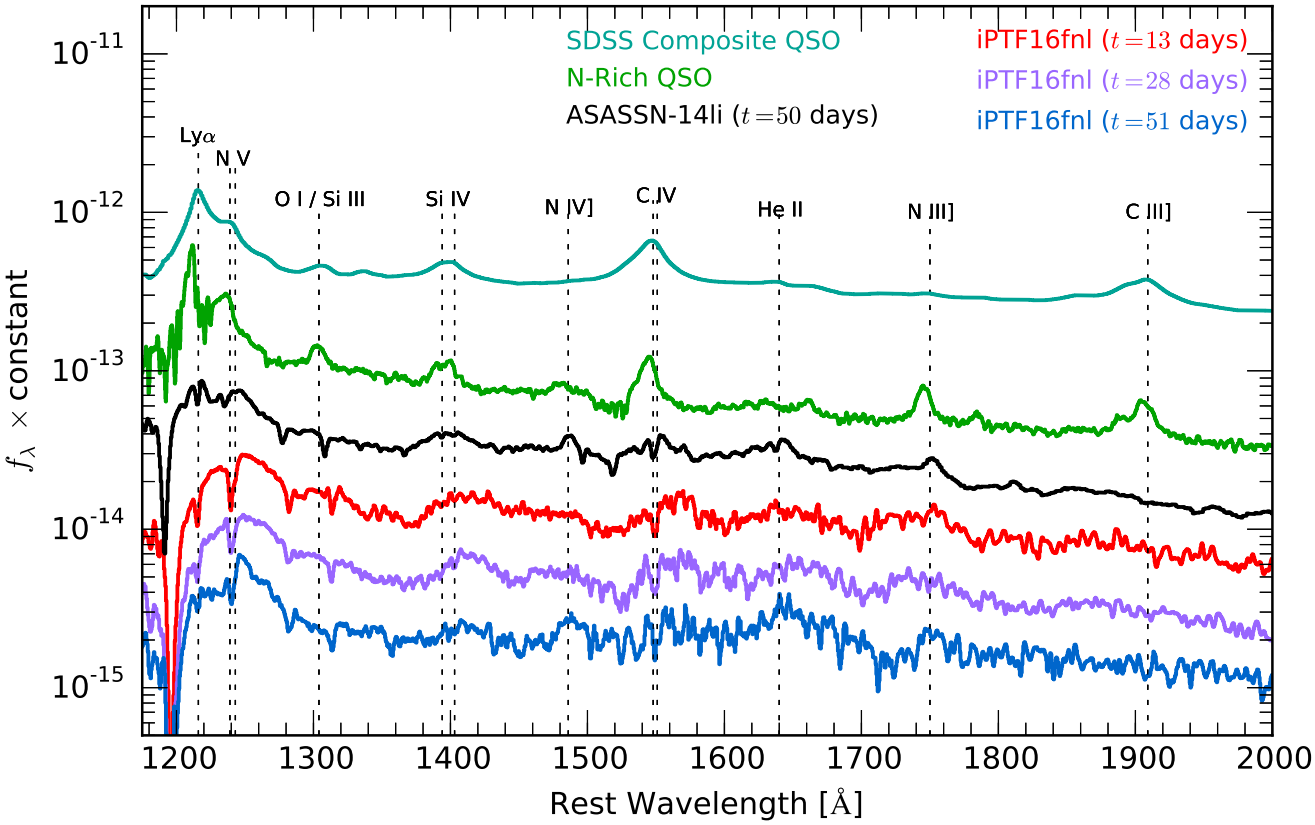

Figure 2. Comparison of the HST/STIS spectral evolution of iPTF16fnl (colored lines) with the HST/STIS spectrum of ASASSN-14li from Cenko et al. (2016) (black), a nitrogen rich quasar (Batra & Baldwin 2014), and the composite quasar spectrum of Vanden Berk et al. (2001). Spectra have been offset by a constant factor for clarity. Prominent features associated with atomic transitions are labeled. Each spectrum is shown in the rest frame of the respective object. The Galactic absorption features appearing in both iPTF16fnl and ASASSN-14li spectra appear at bluer wavelengths in the spectrum of ASASSN-14li due to the different redshifts of the objects.

only weak He I emission, which has a slightly higher ionization energy than Mg II ($E_{\rm ion}$ = 24.59 eV). We also note that there is no C III] emission in any of the TDE spectra. This line is generally used to constrain the density of the broad line region in AGN to $n \lesssim 10^9$ cm^{-3} (Ferland et al. 1992; Peterson 1997), since at higher densities the line is suppressed by collisional deexcitation. The absence of this feature from the TDE spectra may be due to the high density of the emitting material, which would have direct implications for the modeling of TDEs.

Despite these differences between the QSO and TDE spectra, the N-rich QSO spectrum from Batra & Baldwin (2014) bears some striking similarities to the UV spectra of TDEs. While this has been previously noted for the UV spectrum of ASASSN-14li (Kochanek 2016a; Cenko et al. 2016), the strong N features are also present in the spectra of iPTF16fnl. The prevalence of the N lines in the spectra of TDEs further suggests a link between the population of N-rich QSOs and TDEs (Kochanek 2016a).

The optical spectra of iPTF16fnl taken at t = 9, 10, 13, 65, and 81 days are shown in Figure 3. The spectra are qualitatively similar to observations of other TDEs (e.g. Arcavi et al. 2014; Holoien et al. 2014; Brown et al. 2016a), which show a strong blue continuum and broad emission features associated with H and He recombination. Blagorodnova et al. (2017) also present optical spectra of iPTF16fnl that show these same features typically associated with TDEs. The emission line profiles in iPTF16fnl are relatively broad, the host galaxy is bright, and the TDE itself is faint, causing the optical lines to appear relatively weak. In the spectrum taken at t = 13 days the He II λ4686Å feature is quite prominent. This change may in part be due to a narrowing of the line profile, but it is most easily explained by varying levels of host contamination between the observations and across multiple instruments.

While it is challenging to cleanly separate the TDE emission features in our optical spectra, the He II feature is broad and has a substantial amount of flux blueward of 4686Å. This is most evident in the spectrum taken $\sim$ 13 days after discovery and is also quite evident in several spectra from Blagorodnova et al. (2017). The origin of these two components not obvious. The most straightforward interpretation is that both features arise from He II λ4686 with one component blueshifted by $\sim$ 3000 km s^{-1} relative to a component centered at the wavelength of the He II transition. The structure of the stellar debris in TDEs is not well understood, and the kinematics inferred from the line profiles may be useful for constraining the distribution of of the

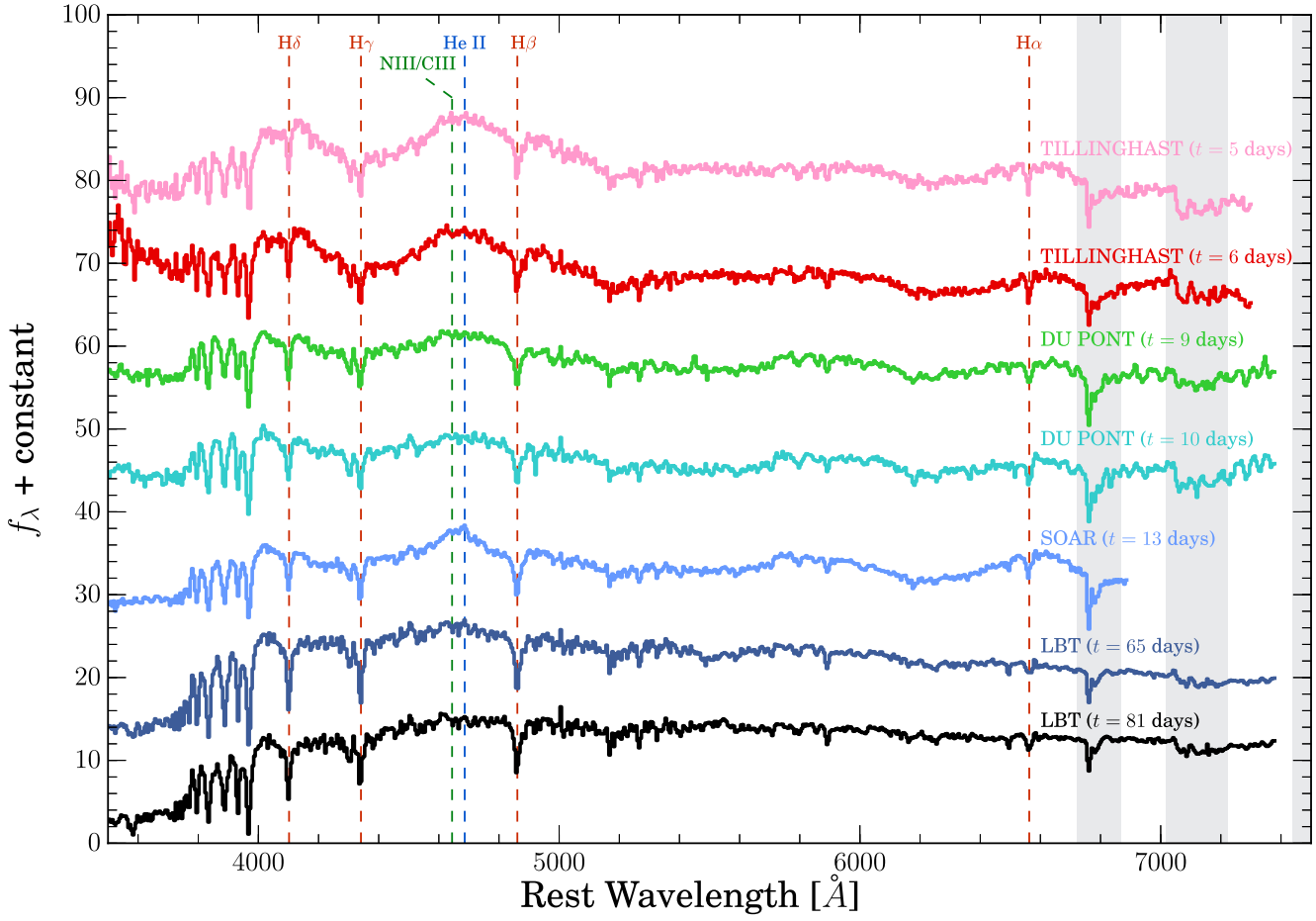

Figure 3. Optical spectral evolution of iPTF16fnl. Color denotes days since discovery. Prominent atomic transitions are labeled, and the shaded regions show the location of telluric features where systematic errors may be significant. The strength of the blue continuum and emission line features decrease with time. The latest spectrum taken with MODS/LBT closely resembles that of a post-starburst galaxy; there is little evidence for residual TDE emission.

emitting material. Arcavi et al. (2014) was able to fit the asymetric double peaked Hα profile of the TDE PTF09djl using a Keplerian disk model from Strateva et al. (2003). However, such a model cannot explain the He II profile in iPTF16fnl because the emission lines in the UV (including He II) do not show the kinematic structure associated with such a disk.

Other TDEs have shown apparent double peaked He II profiles. The most striking example of this is seen in the spectra of ASASSN-14li (Holoien et al. 2016b). The spectra have two strongly peaked line profiles near He II, at approximately 4686Å and 4640Å. In fact, in the earliest spectra of ASASSN-14li, the feature at $\sim$ 4640Å is significantly stronger than the the feature at $\sim$ 4686Å. After $\sim$ 60 days, the anomalous blue feature fades rapidly, and the component at 4686Åremains the stronger of the two for several hundred days (Brown et al. 2016b). Similarly, the H-poor TDE PS1-10jh (Gezari et al. 2012, 2015) also had a He II λ4686Å profile with a significant blue wing, but in that case the peak of the second component was much bluer ($\sim$ 4470Å) than that observed in the TDEs discussed here. Evidence for this second emission feature is seen in other TDEs as well (e.g. ASASSN-14ae, PTF09ge), but its presence is more ambiguous than in ASASSN-14li.

Given the new information afforded by the HST/STIS UV spectra, it seems likely that the feature at $\sim$ 4640Å is in fact due to highly ionized metal lines associated with C III, N III, and possibly N V as well. Gezari et al. (2015) suggested that the blue wing in the He II profile of PS1-10jh could be due to blue shifted C III/N III Wolf-Rayet blends (Niemela, Ruiz & Phillips 1985; Massey & Johnson 1998; Leonard et al. 2000). These lines (including N V) are also prominent in the spectra of the flash ionized material surrounding core collapse supernovae (Shivvers et al. 2015; Gal-Yam et al. 2014; Khazov et al. 2016; Yaron et al. 2017). The complexity of the He II profiles of most optically discovered TDEs suggests that these C III and N III features are actually quite common, and could exacerbate the apparent He/H ratios observed in many TDEs. These features may serve as useful probes of the UV emission when space-based UV observations are not possible, but rapid spectroscopic follow-up of TDEs in both the UV and optical is needed to precisely characterize how they relate to the emission features in the UV.

It is now clear that TDEs frequently have emission features associated with highly ionized metals. In AGN, the highly ionized lines (e.g. C IV) typically have blueshifted line profiles (e.g. Vanden Berk et al. 2001; Richards et al. 2002), and this is clearly seen in the composite quasar spectrum in Figure 2. The apparent blue shift is thought to arise from a relative absence of red flux due to the geometry of AGN and resulting opacity effects. This systematic blueshift is not observed in iPTF16fnl; the highly ionized metal lines are redshifted relative to the systemic velocity. In fact, the emission line profiles in TDEs show a variety of velocity offsets that evolve on a relatively short timescale (e.g. Brown et al. 2016a,b). Additionally, ASASSN-15oi appeared to show varying Doppler shifts between different ionic species (Holoien et al. 2016a). Thus the varying Doppler shifts of the lines are likely to be partially associated with the geometry of the event and the resulting kinematics of the emitting material, rather than being driven only by opacity effects. Such rapid kinematic evolution is not surprising. For example, material at $r = 10^{15} r_{15}$ cm from a SMBH with mass $M_{BH} = 10^6 M_{\rm BH6}$ $M_\odot$ has a characteristic velocity of $v = (GM/r)^{1/2} \sim 3000 M_{\rm BH6}^{1/2} r_{15}^{-1/2}$ km s^{-1}, and the timescale for gravitational accelerations to significantly change the velocity is of order $t \sim 33 r_{15}^{3/2} M_{\rm BH6}^{-1/2}$ days.

When the late-time MODS spectra were taken the TDE had largly vanished in the optical, and the resulting spectra show no clear signs of TDE emission. The spectra closely resemble that of a post-starburst galaxy (e.g., Dressler & Gunn 1983; Zabludoff et al. 1996). The Hδ absorption is quite strong (EW$_{\rm H_\delta}$ $\sim$ -5Å), and there are no signatures of significant ongoing star formation. This is fully consistent with the SED modeling, and places this galaxy firmly in the E+A classification. Thus, iPTF16fnl serves as an additional piece of evidence that TDEs are preferentially found in post-starburst galaxies (French, Arcavi & Zabludoff 2016b,a).

The spatial resolution of our optical spectra is limited to $\sim 1\farcs2$ due to a combination modest observing conditions and slit widths. However, the configuration of the most recent LBT/MODS observation on 2016-11-18 allowed us to align the slit with the major axis of the host galaxy and perform multiple extractions along the slit out to $\pm 6''$ (corresponding to a physical scale of ~ 2 kpc). In the spectra extracted near the galaxy center (Figure 3), there is relatively weak O III λ5007Å emission line. The strength of this nebular feature relative to the stellar continuum increases with distance from the center of the galaxy. Beyond ~ 2 kpc, the S/N of both the stellar continuum and nebular emission decrease rapidly. While the stellar absorption features show clear velocity structure due to the rotation of the disk, there is very little evidence of any kinematic signature in the emission profiles associated with the nebular gas. The LBT/MODS spectrum from 2016-11-02, despite being misaligned with the major axis of the galaxy by $\sim$ 45 degrees, also shows spatially extended nebular emission. While the S/N is relatively low, it appears that the nebular emission probed by this slit orientation does in fact show kinematic structure. It is not unprecedented for the kinematic signatures of the gas to differ from that of a galaxy's stellar population (e.g. Sarzi et al. 2006; Davis et al. 2011; Jin et al. 2016). Similarly, Prieto et al. (2016) showed the host of ASASSN-14li to have spatially extended, filamentary nebular emission well outside the optical extent of the galaxy. In the case of ASASSN-14li, the origin and structure of the nebular gas is most likely related to a merger event (Prieto et al. 2016; Romero-Cañizales et al. 2016), which may explain why TDEs are preferentially found in post-starburst galaxies (French, Arcavi & Zabludoff 2016b,a). Future integral field observations of TDE hosts are necessary to characterize the prevalence of disturbed nebular gas around these unusual galaxies.

3.2 Photometric Analysis

With a combination of *Swift* and ground-based telescopes, we monitored iPTF16fnl continuously for the ~ 120 days following discovery in the near-UV through optical bandpasses. In Figure 4 we show the photometric evolution of iPTF16fnl in the UVOT bands as well as the ground-based observations from Post Observatory. The horizontal dashed lines show the UVOT host magnitudes synthesized from the SED fit to the GALEX (NUV), SDSS (u', g', r', i', and z'), and 2MASS (J, H, K_s) archival data. The vertical marks along the time-axis show the dates corresponding to our spectroscopic observations. The extensive archival data (in particular the GALEX observations) allows us to constrain the host SED quite well. We estimate the accuracy of our synthetic host magnitudes with a bootstrapping scheme in which we perturb the input fluxes by their 1-σ errors and fit the resulting SED. We perform 1000 realizations and find that the resulting magnitude estimates are accurate to within ~ 0.1 mag, which is much smaller than the UV excess in the bluest UVOT bands at later times. The flux in excess of that the host galaxy decreases as one moves toward redder filters, and the photometry in the optical bands is consistent with the host magnitudes only ~ 20 days after discovery.

In order to characterize the excess emission, we correct all fluxes for Galactic extinction assuming $R_V = 3.1$ and $A_V = 0.22$ (O'Donnell 1994; Schlafly & Finkbeiner 2011). We then subtract the host flux and model the SED of the flare as a blackbody using MCMC methods (Foreman-Mackey et al. 2013). We fit the W2, M2, W1, and U band fluxes, and exclude the B and V photometry due to the negligible contribution of the TDE in those bands. In the later epochs, we only use the W2, M2, and W1 measurements if excess flux in the U band is not significantly detected.

In Figure 5 we show the temperature evolution of iPTF16fnl inferred from the UV/optical photometry (black circles) relative to ASASSN-14ae, ASASSN-14li, and ASASSN-15oi (open blue circles, filled red squares, and open green squares, respectively). There is marginal evidence for temperature modulation during the first ~ 30 days, but in general the UV/optical continuum is $3-4\times10^4$ K throughout our follow-up campaign. This inference is driven in part by the fact that we lack the wavelength coverage needed to place a strong constraint on the temperature, and so we impose a prior on our fits of $\log(T/K) = 4.5 \pm 0.1$. The temperature evolution is most similar to that of ASASSN-14li, which remained roughly constant, whereas ASASSN-15oi (and ASASSN-14ae to a lesser extent) showed signs of increasing temperature in the weeks following discovery. While the temperature could in principle be higher than

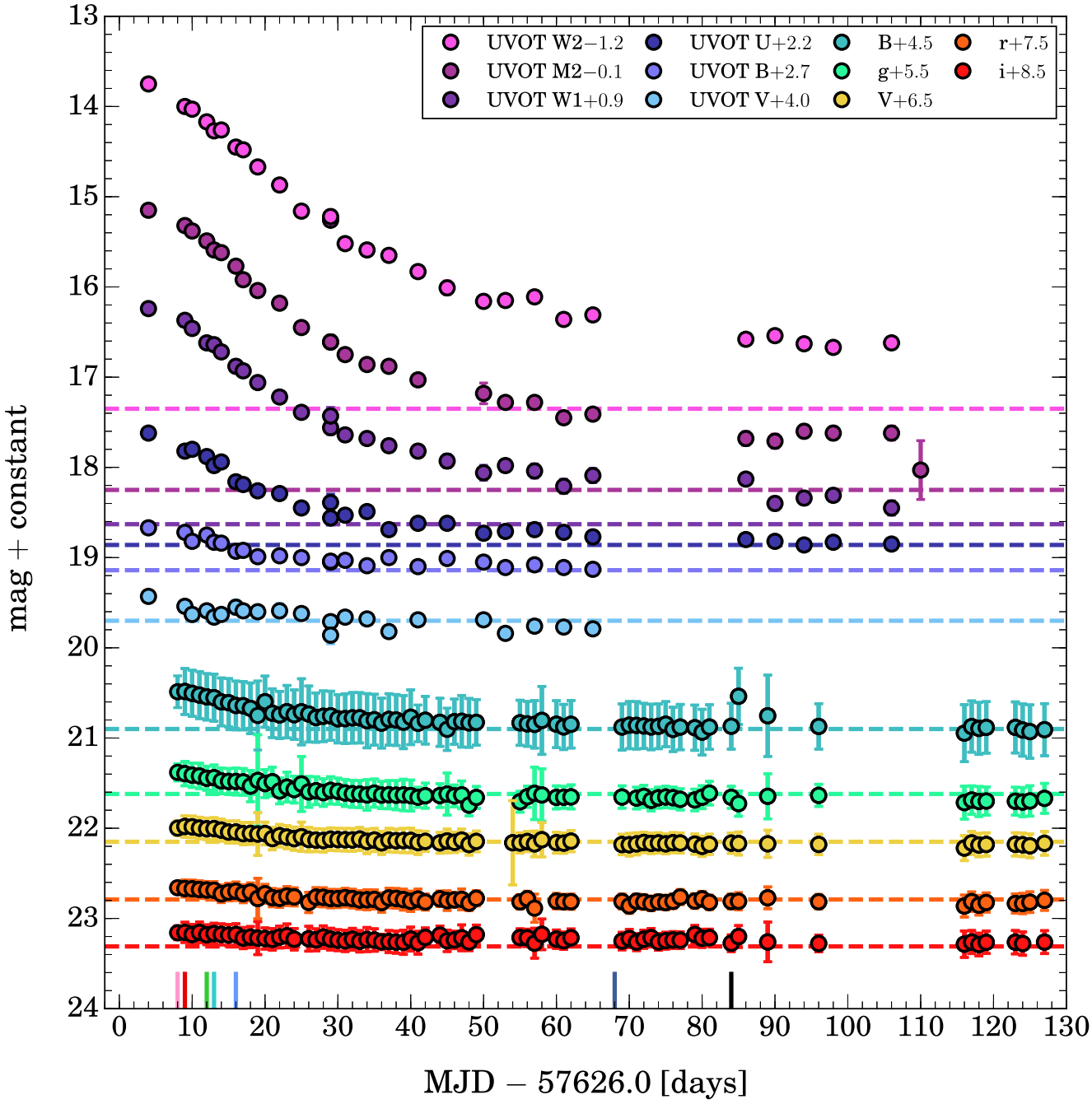

Figure 4. Photometric evolution of iPTF16fnl from discovery to ∼ 130 days after discovery. Circles show the observed non-host-subtracted magnitudes. All UV and optical magnitudes are shown in the Vega system. Horizontal dashed lines show the host magnitudes synthesized from the best fit SED. Like other TDEs, iPTF16fnl remains bright in the UV for significantly longer than in the optical bands, with the bluest bands showing the largest residual flux.

our inferred value, the measurements are largely inconsistent with a lower value.

Figure 6 shows the radial evolution of iPTF16fnl relative to ASAS-SN TDEs. The dashed line shows the radial evolution of a parabolic orbit with closest approach equal to the tidal radius, where $r_g = GM_{\rm BH}/c^2$, and we have adopted a fiducial mass $M_{\rm BH} = 10^7 {\rm M}_\odot$. Overall, the evolution of the photospheric radius in iPTF16fnl is not unlike that of ASASSN-14ae and ASASSN-15oi. The characteristic emitting radius of these three objects decreases by a factor of $\sim 5-10$ within the first ~ 100 days, whereas the radius of ASASSN-14li, which remained luminous for much longer than the other ASAS-SN TDEs, decreases only by a factor of ~ 2. The absolute size of the apparent photospheric radius in iPTF16fnl is in stark contrast with the more luminous ASAS-SN TDEs. The radius peaks at only a few thousand $R_\odot$ and rapidly declines after ~ 10 days. While we have used the term "radius" here, it is unlikely the TDE debris is

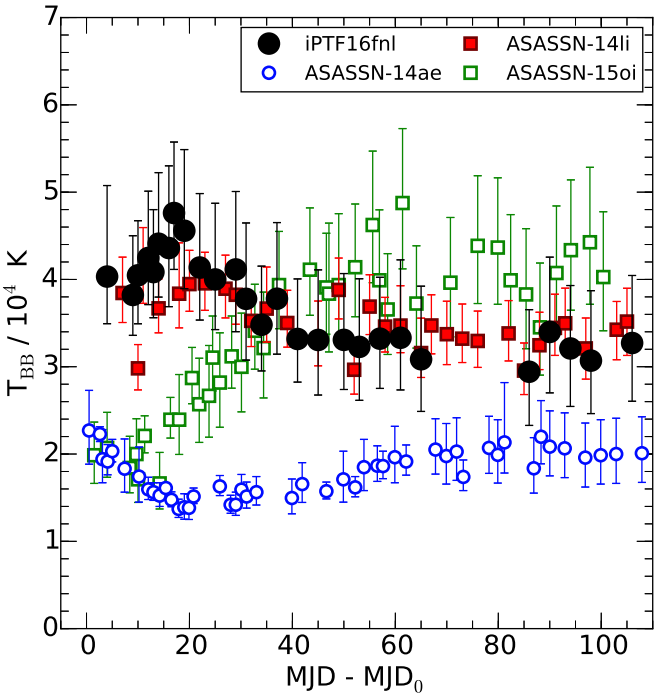

Figure 5. Temperature evolution of iPTF16fnl. Black circles show the temperature of the UV/optical continuum of iPTF16fnl inferred from our blackbody fits to the host subtracted UVOT fluxes. The open blue circles, filled red squares, and open green squares show the temperature evolution of ASASSN-14ae, ASASSN-14li, and ASASSN-15oi, respectively.

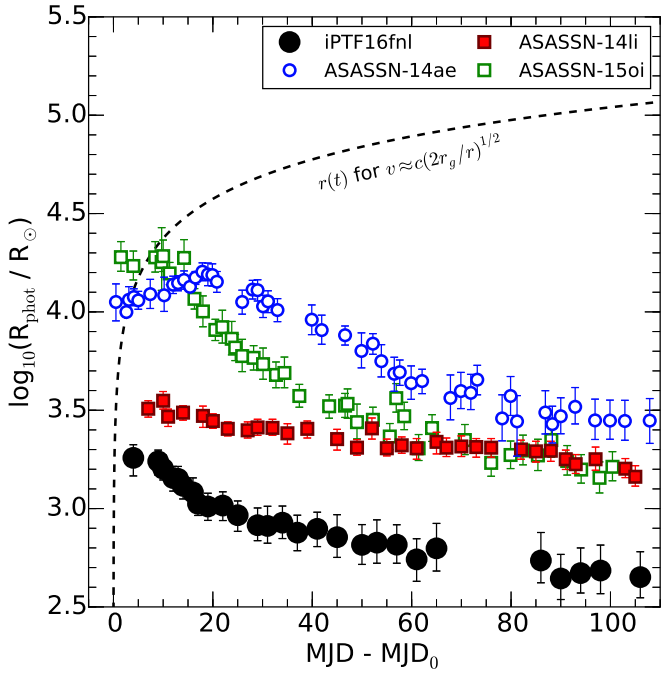

Figure 6. Radius evolution of iPTF16fnl. Black circles show the bolometric luminosity of iPTF16fnl inferred from our blackbody fits to the host subtracted UVOT fluxes; the open blue circles, filled red squares, and open green squares show the radius evolution of ASASSN-14ae, ASASSN-14li, and ASASSN-15oi, respectively. The dashed line shows the evolution of a parabolic orbit with a closest approach equal to the tidal radius for a $10^7 M_\odot$ SMBH. The optical photosphere of iPTF16fnl is significantly smaller than those of the three ASAS-SN TDEs.

actually spherically distributed. In any case, it is clear that the emitting surface of iPTF16fnl is smaller and decreases more rapidly than other optically discovered TDEs.

We estimate the bolometric luminosity by integrating the fits to the SED of the flare for each of our SWIFT epochs, and derive confidence intervals based on the values containing 68% of the MCMC distribution for each epoch. We show the evolution of the bolometric luminosity as black circles in Figure 7. At the earliest phases, iPTF16fnl is a factor of few fainter than the ASAS-SN TDEs and decreases in luminosity by a factor of $\sim 20-30$ over the course of the following weeks. Approximately 50 days after discovery, the decline rate slows, and the emission fades by an additional factor of ~ 2 between 50 and 100 days after discovery. The combination of a low peak luminosity and rapid decline results in iPTF16fnl being a factor of ~ 10 less luminous than the ASAS-SN TDEs after 100 days.

We do not detect X-ray emission in any epoch, and the proximity of iPTF16fnl allows us to place relatively strong constraints on the X-ray emission. In order to derive upper limits on the X-ray flux, we adopt a characteristic X-ray temperature of 5×10^5 K, as we found for ASASSN-14li (Brown et al. 2016b). We correct for Galactic absorption assuming a column density of 5.6×10^{20} cm^{-2} (Kalberla et al. 2005). The downward arrows in Figure 7 denote the upper limits on the X-ray emission from iPTF16fnl. We perform a similar exercise assuming a $\Gamma = 2$ power-law spectrum rather than a blackbody. This provides upper limits which are a factor of ~ 2 smaller. Given the lack of constraints on the true X-ray spectrum, we adopt the relatively conservative limits derived assuming a blackbody emission spectrum, which are still a factor of ~ 5 more stringent than those obtained for ASASSN-14ae and ASASSN-15oi. At early times, our limits require that the X-ray luminosity be $< 1\%$ of the UV/optical luminosity. This is in stark contrast with ASASSN-14li, in which the X-ray luminosity remained comparable to the UV/optical luminosity for several hundred days (Holoien et al. 2016b; Brown et al. 2016b).

In Figure 8 we show the SED of iPTF16fnl at the same three epochs shown in Figure 1, and the color scheme is the same as that used in earlier plots to denote the observation dates. The colored squares show the host-subtracted *Swift* fluxes corrected for Galactic extinction, and the solid lines show our blackbody fits to data. The dashed lines show similar blackbody models but with the temperature fixed at $T = 2 \times 10^4$ K and an increased normalization. In general, the *Swift* fluxes are better described with a relatively hot blackbody rather than the cooler models.

Figure 8 also shows constraints on the luminosity at short wavelengths derived from the X-ray limits and the He II optical line flux. In order to improve the constraints on the X-ray flux beyond the single epoch limits shown in Figure 7, we stack the individual exposures. We obtain a flux limit of $\sim 1.1 \times 10^{-13}$ ergs s^{-1} cm^2 corresponding to a luminosity of $L \sim 1.3 \times 10^7 L_\odot$, which we show as the downward pointing triangle. Following Holoien et al. (2014) we

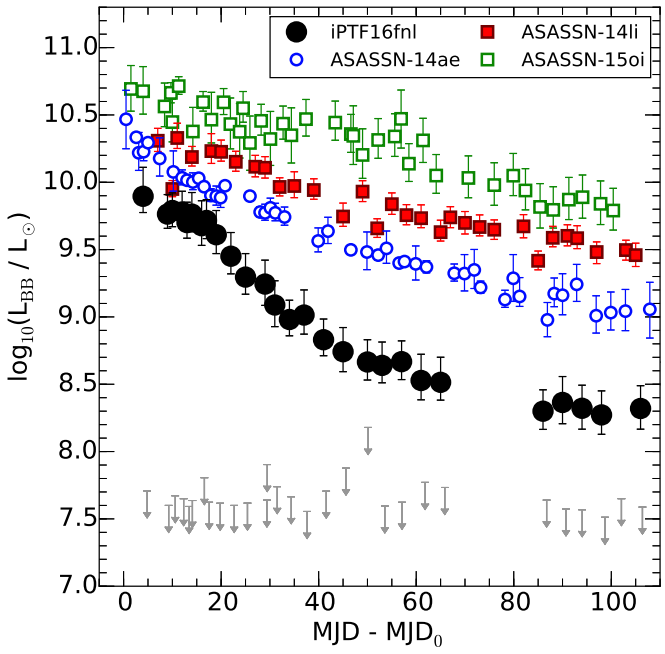

Figure 7. Luminosity evolution of iPTF16fnl. Black circles show the bolometric luminosity of iPTF16fnl inferred from our blackbody fits to the host subtracted UVOT fluxes; the open blue circles, filled red squares, and open green squares show the temperature evolution of ASASSN-14ae, ASASSN-14li, and ASASSN-15oi, respectively. The bolometric luminosity of iPTF16fnl is significantly lower than that of the ASAS-SN TDEs.

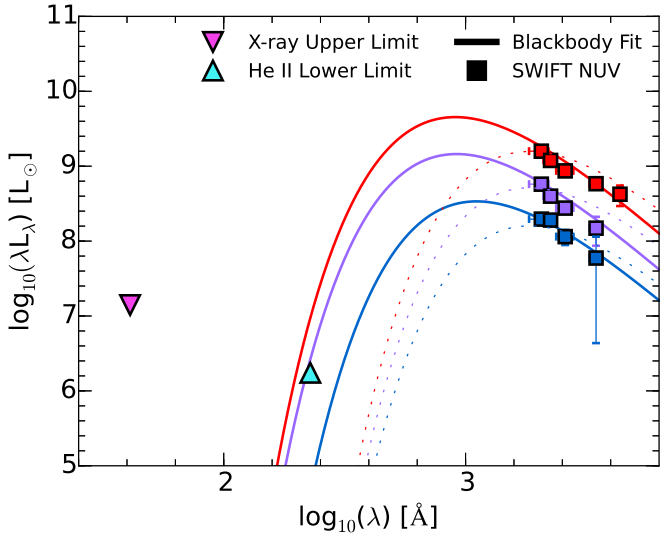

Figure 8. Spectral energy distribution of iPTF16fnl. The colored squares show the host-subtracted *Swift* fluxes corrected for Galactic extinction. The solid lines show our blackbody fits to the TDE flux; the dashed lines show similar blackbody models but with the temperature fixed at $T = 2 \times 10^4$ K. The downward and upward arrows show the flux limits inferred from our X-ray and optical spectroscopic observations, respectively.

use the flux of the He II λ4686Å line to infer a lower limit on the He II ionizing luminosity, which we show in Figure 8 as the upward pointing triangle. However, this assumes that the material is optically thin to the He II emission, and that the He II emission arises from a balance of photoionization and recombination. Roth et al. (2016) argue that for reasonable physical conditions, the optical depth of the TDE debris in the Hα line can be be significant. Furthermore, given the presence of the collisionally excited resonance lines in the UV, collisional ionization of H may be significant. Thus these assumptions are unlikely to be true for H, but should be more appropriate for He II. The He II line flux is highly uncertain, but we can still infer an approximate lower limit. Over the course of the observations we measure a He II flux corresponding to a luminosity $\gtrsim 10^{40}$ ergs s^{-1} in the early epochs and $\lesssim 10^{39}$ ergs s^{-1} in the later epochs. We adopt a conservative lower limit of 10^{39} ergs s^{-1} for the He II λ4686Å luminosity, and note that decreasing the lower limit by an additional order of magnitude would have no impact on our conclusions. The limits on the X-ray luminosity are quite strong and rule out the presence of a soft ($T \sim 5 \times 10^5$ K) X-ray source down to $\sim 10^7$ L$_\odot$. On the other hand, the He II λ4686Å flux requires a non-negligible amount of flux near 200Å. Our $\sim 3 \times 10^4$ K blackbody models produce enough ionizing flux to power the He II line, while the cooler blackbody models (dashed lines) do not produce enough ionizing flux on their own. However, the X-ray limits are not so stringent as to rule out the presence of a soft X-ray component with enough ionizing flux to power the He II λ4686Å line. In fact, the optical line fluxes of other TDEs appear to require an additional source of ionization beyond a simple UV/optical blackbody (Holoien et al. 2014; Roth et al. 2016; Holoien et al. 2016a).

There is some tension between the results presented here and those presented in Blagorodnova et al. (2017). First, we systematically favor a higher blackbody temperature ($\gtrsim 3 \times 10^4$ K instead of 2×10^4 K). This appears to be driven by the assumption in Blagorodnova et al. (2017) that the late time flux is dominated by the host galaxy. We find that there is still a significant contribtion to the UV flux from the TDE at late times, as shown in Figure 4. This is corroborated by the fact that the late-time *Swift* W2 flux is ~ 1 magnitude brighter than the comparable archival GALEX NUV flux. Overestimating the UV flux of the host will naturally drive the temperature estimate downward. We also adopt a slightly higher Galactic extinction ($A_V = 0.22$ instead of $A_V = 0.19$), but this is a secondary effect. The second difference is that Blagorodnova et al. (2017) claim an X-ray detection. In our analysis, the *Swift* counts associated with the source are consistent with a background fluctuation, assuming Poisson statistics. Given the low X-ray flux of the detection reported by Blagorodnova et al. (2017), this has no practical impact on our conclusion that the X-rays are not an energetically important component of the observed fluxes.

4 CONCLUSIONS

We presented for the first time the UV spectroscopic evolution of a TDE using data from HST/STIS. We have shown that the shape and velocity offset of the broad UV emission

and absorption features evolve with time. While the UV spectra closely resemble that of ASASSN-14li (Cenko et al. 2016), there is little qualitative resemblance to the UV spectra of typical quasars. However, there are some similarities between the of the UV spectra of iPTF16fnl, ASASSN-14li, and N-rich quasars (Batra & Baldwin 2014), which further suggests that there may be a link between N-rich quasars and TDEs (Kochanek 2016a). While the UV line profiles are significantly blended, future higher signal-to-noise observations of brighter TDEs will permit a more quantitative assessment of the line evolution.

The optical spectra of iPTF16fnl resemble those of several other optically discovered TDEs. Given the emission features in the UV, it seems likely that the anomolous emission features just blueward of He II λ4686Å that have been observed in many TDEs are in fact due to N III and C III Wolf-Rayet blends. These features may contaminate He II λ4686Å, which would make them partly responsible for the large He/H ratios inferred in some TDEs. However, they could also serve as indirect probes of the UV emission when space based observations are not possible. Prompt, high signal-to-noise UV and optical spectra of TDEs are needed before a robust connection between the two can be established.

We monitored the TDE for over 100 days using the *Swift* space telescope and used the XRT and UVOT observations to characterize the broadband SED of the TDE. We showed that the characteristic temperature of the UV/optical emission was $\gtrsim 3 \times 10^4$ K and remained relatively constant over the course of our 100 day observing campaign. Interestingly, the TDE remained dim and faded rapidly relative to other optically discovered TDEs. This is presumably due to an unusually small emitting surface compared to other TDEs. Integrating the UV/optical luminosity over the course of our observing campaign, the total energy radiated by iPTF16fnl is $\sim 5 \times 10^{49}$ ergs, which is approximately an order of magnitude less than the ASAS-SN TDEs found to date. This corresponds to a small fraction of a solar mass of accreted matter: $\Delta M \sim 3 \times 10^{-4} \eta_{0.1}^{-1} \mathrm{M}_\odot$, where $\eta_{0.1}$ is the radiative efficiency relative to 0.1. Despite the low luminosity of the TDE, we obtain strong limits on the X-ray emission and constrain the 0.3–10 keV X-ray luminosity to be $\lesssim 1\%$ that of the UV/optical luminosity. The disparate X-ray properties of iPTF16fnl and ASASSN-14li are somewhat surprising given the similarities in their UV spectroscopic properties.

Given the low luminosity of iPTF16fnl it is likely that there are many TDEs of similar (or lesser) luminosity that are simply undetected by current transient surveys. Kochanek (2016b) argue that if the luminosity function of TDEs scales roughly with the black hole mass function then there should be a large number of relatively low luminosity TDEs around relatively low mass SMBHs that are generally missed by current transient surveys. Given the proximity and low luminosity of iPTF16fnl, it appears that this may indeed be the case. As the current generation of transient surveys matures and the detection efficiencies are better characterized, it should be possible to constrain the approximate luminosity function of TDEs and improve the estimate of the volumetric rate. Accurately characterizing the properties of low luminosity events like iPTF16fnl are a key aspect of determinining the volume corrected statistical properties of TDEs.

ACKNOWLEDGEMENTS

The authors thank Rick Pogge for valuable discussions.

JSB, KZS, and CSK are supported by NSF grants AST-1515876 and AST-1515927.

TW-SH is supported by the DOE Computational Science Graduate Fellowship, grant number DE-FG02-97ER25308.

BJS is supported by NASA through Hubble Fellowship grant HF-51348.001 awarded by the Space Telescope Science Institute, which is operated by the Association of Universities for Research in Astronomy, Inc., for NASA, under contract NAS 5-26555.

Support for JLP is provided in part by FONDECYT through the grant 1151445 and by the Ministry of Economy, Development, and Tourism's Millennium Science Initiative through grant IC120009, awarded to The Millennium Institute of Astrophysics, MAS.

S.V.Jr. is supported by the National Science Foundation Graduate Research Fellowship under Grant No. DGE-1343012.

Based on observations made with the NASA/ESA Hubble Space Telescope, obtained at the Space Telescope Science Institute, which is operated by the Association of Universities for Research in Astronomy, Inc., under NASA contract NAS 5-26555. These observations are associated with program #GO-14781.

This paper used data obtained with the MODS spectrographs built with funding from NSF grant AST-9987045 and the NSF Telescope System Instrumentation Program (TSIP), with additional funds from the Ohio Board of Regents and the Ohio State University Office of Research.

Based on data acquired using the Large Binocular Telescope (LBT). The LBT is an international collaboration among institutions in the United States, Italy, and Germany. LBT Corporation partners are: The University of Arizona on behalf of the Arizona university system; Istituto Nazionale di Astrofisica, Italy; LBT Beteiligungsgesellschaft, Germany, representing the Max-Planck Society, the Astrophysical Institute Potsdam, and Heidelberg University; The Ohio State University, and The Research Corporation, on behalf of The University of Notre Dame, University of Minnesota and University of Virginia.

This research has made use of the XRT Data Analysis Software (XRTDAS) developed under the responsibility of the ASI Science Data Center (ASDC), Italy. At Penn State the NASA *Swift* program is supported through contract NAS5-00136.

This paper uses data products produced by the OIR Telescope Data Center, supported by the Smithsonian Astrophysical Observatory.

Observations made with the NASA Galaxy Evolution Explorer (GALEX) were used in the analyses presented in this manuscript. Some of the data presented in this paper were obtained from the Mikulski Archive for Space Telescopes (MAST). STScI is operated by the Association of Universities for Research in Astronomy, Inc., under NASA contract NAS5-26555. Support for MAST for non-HST data is provided by the NASA Office of Space Science via grant NNX13AC07G and by other grants and contracts.

Funding for SDSS-III has been provided by the Alfred P. Sloan Foundation, the Participating Institutions,

the National Science Foundation, and the U.S. Department of Energy Office of Science. The SDSS-III web site is http://www.sdss3.org/.

This publication makes use of data products from the Two Micron All Sky Survey, which is a joint project of the University of Massachusetts and the Infrared Processing and Analysis Center/California Institute of Technology, funded by NASA and the National Science Foundation.

This publication makes use of data products from the Wide-field Infrared Survey Explorer, which is a joint project of the University of California, Los Angeles, and the Jet Propulsion Laboratory/California Institute of Technology, funded by NASA.

This research is based in part on observations obtained at the Southern Astrophysical Research (SOAR) telescope, which is a joint project of the Ministério da Ciência, Tecnologia, e Inovação (MCTI) da República Federativa do Brasil, the U.S. National Optical Astronomy Observatory (NOAO), the University of North Carolina at Chapel Hill (UNC), and Michigan State University (MSU).

REFERENCES

Alam S. et al., 2015, ApJS, 219, 12
Alard C., 2000, A&AS, 144, 363
Alard C., Lupton R. H., 1998, ApJ, 503, 325
Arcavi I. et al., 2014, ApJ, 793, 38
Assef R. J. et al., 2013, ApJ, 772, 26
Auchettl K., Guillochon J., Ramirez-Ruiz E., 2016, ArXiv e-prints
Batra N. D., Baldwin J. A., 2014, MNRAS, 439, 771
Becker R. H., White R. L., Helfand D. J., 1995, ApJ, 450, 559
Blagorodnova N. et al., 2017, ArXiv e-prints
Breeveld A. A. et al., 2010, MNRAS, 406, 1687
Brown J. S., Shappee B. J., Holoien T. W.-S., Stanek K. Z., Kochanek C. S., Prieto J. L., 2016a, MNRAS, 462, 3993
Brown J. S., W.-S Holoien T., Auchettl K., Stanek K. Z., Kochanek C. S., Shappee B. J., Prieto J. L., Grupe D., 2016b, ArXiv e-prints
Brown T. M. et al., 2013, PASP, 125, 1031
Bruzual G., Charlot S., 2003, MNRAS, 344, 1000
Burrows D. N. et al., 2005, Space Sci. Rev., 120, 165
Cardelli J. A., Clayton G. C., Mathis J. S., 1989, ApJ, 345, 245
Cenko S. B. et al., 2016, ApJ, 818, L32
Condon J. J., Cotton W. D., Greisen E. W., Yin Q. F., Perley R. A., Taylor G. B., Broderick J. J., 1998, AJ, 115, 1693
Cutri R. M., et al., 2014, VizieR Online Data Catalog, 2328
Davis T. A. et al., 2011, MNRAS, 417, 882
Denney K. D., Peterson B. M., Dietrich M., Vestergaard M., Bentz M. C., 2009, ApJ, 692, 246
Dressler A., Gunn J. E., 1983, ApJ, 270, 7
Evans C. R., Kochanek C. S., 1989, ApJ, 346, L13
Fabricant D., Cheimets P., Caldwell N., Geary J., 1998, PASP, 110, 79
Ferland G. J., Peterson B. M., Horne K., Welsh W. F., Nahar S. N., 1992, ApJ, 387, 95
Foreman-Mackey D., Hogg D. W., Lang D., Goodman J., 2013, PASP, 125, 306
French K. D., Arcavi I., Zabludoff A., 2016a, ArXiv e-prints
French K. D., Arcavi I., Zabludoff A., 2016b, ApJ, 818, L21
Gal-Yam A. et al., 2014, Nature, 509, 471
Gezari S., Chornock R., Lawrence A., Rest A., Jones D. O., Berger E., Challis P. M., Narayan G., 2015, ApJ, 815, L5
Gezari S. et al., 2012, Nature, 485, 217
Gezari S. et al., 2016, The Astronomer's Telegram, 9433
Grupe D., Thomas H.-C., Leighly K. M., 1999, A&A, 350, L31
Henden A. A., Templeton M., Terrell D., Smith T. C., Levine S., Welch D., 2016, VizieR Online Data Catalog, 2336
Hill J. E. et al., 2004, in Proc. SPIE, Vol. 5165, X-Ray and Gamma-Ray Instrumentation for Astronomy XIII, Flanagan K. A., Siegmund O. H. W., eds., pp. 217–231
Holoien T. W.-S. et al., 2016a, http://arxiv.org/abs/1602.01088
Holoien T. W.-S. et al., 2016b, MNRAS, 455, 2918
Holoien T. W.-S. et al., 2014, MNRAS, 445, 3263
Jin Y. et al., 2016, MNRAS, 463, 913
Kalberla P. M. W., Burton W. B., Hartmann D., Arnal E. M., Bajaja E., Morras R., Pöppel W. G. L., 2005, A&A, 440, 775
Khazov D. et al., 2016, ApJ, 818, 3
Kochanek C. S., 2016a, MNRAS, 458, 127
Kochanek C. S., 2016b, MNRAS, 461, 371
Komossa S., Bade N., 1999, A&A, 343, 775
Komossa S., Greiner J., 1999, A&A, 349, L45
Kriek M., van Dokkum P. G., Labbé I., Franx M., Illingworth G. D., Marchesini D., Quadri R. F., 2009, ApJ, 700, 221
Leonard D. C., Filippenko A. V., Barth A. J., Matheson T., 2000, ApJ, 536, 239
Martin D. C. et al., 2005, ApJ, 619, L1
Massey P., Johnson O., 1998, ApJ, 505, 793
McConnell N. J., Ma C.-P., 2013, ApJ, 764, 184
McGill K. L., Woo J.-H., Treu T., Malkan M. A., 2008, ApJ, 673, 703
Niemela V. S., Ruiz M. T., Phillips M. M., 1985, ApJ, 289, 52
O'Donnell J. E., 1994, ApJ, 422, 158
Peterson B. M., 1993, PASP, 105, 247
Peterson B. M., 1997, An Introduction to Active Galactic Nuclei
Phinney E. S., 1989, in IAU Symposium, Vol. 136, The Center of the Galaxy, Morris M., ed., p. 543
Pogge R. W. et al., 2010, in Society of Photo-Optical Instrumentation Engineers (SPIE) Conference Series, Vol. 7735, Society of Photo-Optical Instrumentation Engineers (SPIE) Conference Series
Poole T. S. et al., 2008, MNRAS, 383, 627
Prieto J. L. et al., 2016, ApJ, 830, L32
Rees M. J., 1988, Nature, 333, 523
Richards G. T., Vanden Berk D. E., Reichard T. A., Hall P. B., Schneider D. P., SubbaRao M., Thakar A. R., York D. G., 2002, AJ, 124, 1
Romero-Cañizales C., Prieto J. L., Chen X., Kochanek C. S., Dong S., Holoien T. W.-S., Stanek K. Z., Liu F., 2016, ApJ, 832, L10
Roming P. W. A. et al., 2005, Space Sci. Rev., 120, 95
Roth N., Kasen D., Guillochon J., Ramirez-Ruiz E., 2016, ApJ, 827, 3
Sarzi M. et al., 2006, MNRAS, 366, 1151
Schlafly E. F., Finkbeiner D. P., 2011, ApJ, 737, 103
Shappee B. J. et al., 2014, ApJ, 788, 48
Shivvers I., Groh J. H., Mauerhan J. C., Fox O. D., Leonard D. C., Filippenko A. V., 2015, ApJ, 806, 213
Skrutskie M. F. et al., 2006, AJ, 131, 1163
Stern D. et al., 2012, ApJ, 753, 30
Strateva I. V. et al., 2003, AJ, 126, 1720
Vanden Berk D. E. et al., 2001, AJ, 122, 549
Villanueva S., Eastman J. D., Gaudi B. S., Pogge R. W., Stassun K. G., Trueblood M., Trueblood P., 2016, in Proc. SPIE, Vol. 9906, Ground-based and Airborne Telescopes VI, p. 99062L
Vinkó J. et al., 2015, ApJ, 798, 12
Voges W. et al., 1999, A&A, 349, 389
Yaron O. et al., 2017, ArXiv e-prints
Zabludoff A. I., Zaritsky D., Lin H., Tucker D., Hashimoto Y., Shectman S. A., Oemler A., Kirshner R. P., 1996, ApJ, 466, 104

This paper has been typeset from a TEX/LATEX file prepared by the author.

APPENDIX A: FOLLOW-UP PHOTOMETRY

All UVOT and XRT follow-up photometry is presented in Table A1 below. UVOT photometry is presented in the Vega system, and XRT limits are presented in units of 10^{-3} counts s^{-1}. The data have not been corrected for Galactic absorption.

Table A1. *Swift* Observations.

MJD	XRT Limits [$\times 10^{-3}$ count s^{-1}]	W2	M2	W1	U	B	V
57631	< 3.85	14.95 ± 0.04	15.25 ± 0.04	15.34 ± 0.05	15.42 ± 0.04	15.97 ± 0.03	15.43 ± 0.05
57635	< 3.01	15.20 ± 0.04	15.42 ± 0.03	15.47 ± 0.05	15.62 ± 0.05	16.02 ± 0.04	15.54 ± 0.05
57637	< 3.55	15.23 ± 0.04	15.48 ± 0.03	15.56 ± 0.05	15.60 ± 0.05	16.12 ± 0.04	15.63 ± 0.05
57638	< 3.38	15.37 ± 0.04	15.59 ± 0.04	15.72 ± 0.05	15.68 ± 0.04	16.05 ± 0.04	15.59 ± 0.06
57639	< 2.96	15.47 ± 0.04	15.69 ± 0.03	15.74 ± 0.05	15.78 ± 0.05	16.13 ± 0.04	15.66 ± 0.05
57640	< 3.27	15.46 ± 0.04	15.72 ± 0.03	15.82 ± 0.05	15.74 ± 0.05	16.14 ± 0.04	15.63 ± 0.05
57643	< 4.84	15.65 ± 0.05	15.87 ± 0.05	15.98 ± 0.07	15.96 ± 0.07	16.23 ± 0.06	15.55 ± 0.08
57644	< 3.17	15.68 ± 0.04	16.02 ± 0.04	16.03 ± 0.06	15.99 ± 0.05	16.22 ± 0.04	15.59 ± 0.06
57646	< 3.12	15.87 ± 0.04	16.14 ± 0.04	16.16 ± 0.06	16.06 ± 0.05	16.29 ± 0.04	15.60 ± 0.05
57649	< 3.01	16.07 ± 0.04	16.28 ± 0.05	16.32 ± 0.06	16.09 ± 0.05	16.28 ± 0.04	15.59 ± 0.08
57651	< 3.13	16.36 ± 0.04	16.55 ± 0.04	16.49 ± 0.05	16.25 ± 0.05	16.30 ± 0.04	15.62 ± 0.05
57655	< 3.30	16.46 ± 0.06	16.71 ± 0.06	16.66 ± 0.08	16.36 ± 0.08	16.35 ± 0.05	15.71 ± 0.07
57655	< 6.06	16.42 ± 0.07	16.71 ± 0.08	16.53 ± 0.09	16.19 ± 0.09	16.34 ± 0.07	15.86 ± 0.10
57658	< 4.15	16.72 ± 0.05	16.85 ± 0.05	16.74 ± 0.07	16.33 ± 0.07	16.33 ± 0.05	15.66 ± 0.06
57660	< 3.49	16.79 ± 0.05	16.96 ± 0.05	16.78 ± 0.07	16.29 ± 0.05	16.39 ± 0.04	15.68 ± 0.05
57664	< 2.71	16.85 ± 0.05	16.98 ± 0.05	16.86 ± 0.07	16.49 ± 0.06	16.30 ± 0.04	15.82 ± 0.06
57668	< 3.84	17.03 ± 0.06	17.13 ± 0.05	16.92 ± 0.07	16.42 ± 0.06	16.40 ± 0.04	15.69 ± 0.05
57672	< 5.69	17.21 ± 0.08	...	17.03 ± 0.07	16.42 ± 0.06	16.31 ± 0.05	...
57676	< 11.4	17.36 ± 0.07	17.28 ± 0.11	17.16 ± 0.08	16.53 ± 0.07	16.35 ± 0.05	15.69 ± 0.06
57680	< 2.97	17.35 ± 0.06	17.38 ± 0.06	17.08 ± 0.07	16.51 ± 0.06	16.41 ± 0.04	15.84 ± 0.06
57683	< 3.17	17.31 ± 0.07	17.38 ± 0.06	17.14 ± 0.08	16.49 ± 0.07	16.38 ± 0.05	15.76 ± 0.06
57688	< 4.45	17.56 ± 0.07	17.55 ± 0.06	17.31 ± 0.08	16.52 ± 0.06	16.41 ± 0.04	15.77 ± 0.05
57692	< 4.09	17.51 ± 0.07	17.51 ± 0.07	17.19 ± 0.08	16.57 ± 0.07	16.43 ± 0.04	15.79 ± 0.06
57713	< 3.29	17.78 ± 0.06	17.78 ± 0.08	17.23 ± 0.06	16.60 ± 0.05	...	...
57717	< 2.84	17.74 ± 0.06	17.81 ± 0.08	17.50 ± 0.07	16.62 ± 0.05	...	...
57720	< 2.79	17.83 ± 0.06	17.70 ± 0.07	17.44 ± 0.07	16.66 ± 0.05	...	...
57725	< 2.45	17.87 ± 0.06	17.72 ± 0.07	17.41 ± 0.07	16.63 ± 0.05	...	...
57728	< 3.38	...	...	...	...	...	...
57732	< 2.92	17.82 ± 0.06	17.72 ± 0.08	17.55 ± 0.08	16.65 ± 0.05	...	...
57737	< 34.8	...	18.13 ± 0.33	...	...	...	...

Magnitudes and uncertainties are presented in the Vega system. X-ray count rate limits are given in units of 10^{-3} counts per second in the energy range $0.3 - 10$ keV. Data are not corrected for Galactic absorption.